Characterization of Multicellular Niches Supporting Hematopoietic Stem Cells Within Distinct Zones

Ruochen Dong[1], Hua Li[1], Xi C He[1], Chen Wang[2], Anoja Perera[1], Seth Malloy[1], Jonathon Russell[1], Wenting Li[1], Kaitlyn Petentler[1], Xinjian Mao[1], Zhe Yang[1], Michael Epp[1], Kate Hall[1], Allison Scott[1], Mary C. McKinney[1], Shengping Huang[1], Sarah E Smith[1], Mark Hembree[1], Yongfu Wang[1], Zulin Yu[1], Jeffery S. Haug[1], Jay Unruh[1], Brian Slaughter[1], Xunlei Kang[2], Linheng Li[1,3,4*]

[1]Stowers Institute for Medical Research, Kansas City, MO 64110, USA

[2] Division of Hematology and Oncology, Department of Medicine, University of Missouri School of Medicine, Columbia, MO 65212, USA

[3]Department of Pathology & Laboratory Medicine, Division of Molecular Oncology, University of Kansas Medical Center, Kansas City, Kansas, 66160, USA

[4]Lead Contact

*Correspondence: lil@stowers.org (L.L.)

Abstract

Previous studies of hematopoietic stem cells (HSCs) primarily focused on single cell-based niche models, yielding fruitful but conflicting findings[1-5]. Here we report our investigation on the fetal liver (FL) as the primary fetal hematopoietic site using spatial transcriptomics. Our study reveals two distinct niches: the portal-vessel (PV) niche and the sinusoidal niche. The PV niche, composing N-cadherin (N-cad)^{Hi}Pdgfrα^{+} mesenchymal stromal cells (MSCs), endothelial cells (ECs), and N-cad^{Lo}Albumin^{+} hepatoblasts, maintains quiescent and multipotential FL-HSCs. Conversely, the sinusoidal niche, comprising ECs, hepatoblasts and hepatocytes, as well as potential macrophages and megakaryocytes, supports proliferative FL-HSCs biased towards myeloid lineages. Unlike prior reports on the role of Cxcl12, with its depletion from vessel-associated stromal cells leading to 80% of HSCs' reduction in the adult bone marrow (BM)[6,7], depletion of *Cxcl12* via *Cdh2*^{CreERT} (encoding N-cad) induces altered localization of HSCs from the PV to the sinusoidal niches, resulting in an increase of HSC number but with myeloid-bias. Similarly, we discovered that adult BM encompasses two niches within different zones, each composed of multi-cellular components: trabecular bone area (TBA, or metaphysis) supporting deep-quiescent HSCs, and central marrow (CM, or diaphysis) fostering heterogenous proliferative HSCs. This study transforms our understanding of niches by shifting from single cell-based to multicellular components within distinct zones, illuminating the intricate regulation of HSCs tailored to their different cycling states.

Introduction

Hematopoietic stem cells (HSCs) possess the remarkable self-renew ability and multilineage potential, ensuring a lifelong supply of both HSCs and lineage cells[8]. Definitive HSCs emerge from the hemogenic endothelium in the aorta-gonad-mesonephros (AGM) region around E10.5-11.5 and subsequently migrate to the FL after E12.5 for expansion. The FL serves as the primary site for HSC maturation and expansion[9-12]. It is estimated that HSCs undergo a 38-fold expansion between E12

and E18 in the FL before migrating to the BM near birth to support lifelong hematopoiesis in adults[13-15].

In the adult BM, it was proposed that HSCs reside within physically confined microenvironment or niche[16], however the identification of the cell types that serve as niches in supporting HSCs within the BM has been a long journey over the past two decades[1-4,17]. The first HSC niche was found in the TBA or metaphysis as evidenced by the observations that increased TBA led to an increased HSC number[18,19], thus forming the concept of the endosteal (inner bone surface) niche. Notably, in these studies, long-term (LT) quiescent HSCs were identified using two criteria: 1) LT BrdU labeling (for 10-days) followed by a 70-day chase to detect label-retaining cells (LRCs), and 2) HSC markers $Lin^{-}CD45^{+}Sca1^{+}Kit^{+}$ expression in a subset of LRCs. Within the increased TBA, more N-cad^{+} bone-lining cells correlates with more $LRC^{+}Lin^{-}CD45^{+}Sca1^{+}Kit^{+}$ HSCs[18,20]. It is important to acknowledge that employing different LRC procedures, including variations in labeling and chasing time, may result in the identification of different cell status or even cell types[21]. This is because each division of HSCs diminishes their labels such as BrdU or GFP and their self-renewal capacity, and it should be noted that not all LRCs necessarily correspond to HSCs[22,23]. Moreover, these LT quiescent HSCs were primarily found in the endosteal region (70-75%) and within the TBA, many of which were observed adjacent to N-cad^{+} bone-lining cells, although the exact nature of the latter was not fully understood at the time[18,20,22]. Functionally, through the utilization of real-time imaging technology, transplanted HSCs were often detected homing to the endosteal region, particularly to the N-cad^{+} niche within the TBA[24,25]. With the identification of improved HSC markers, $Lin^{-}CD150^{+}CD48^{-}CD41^{-}$, the more accurate mapping the location of HSCs became possible as 1 out of 3 $CD150^{+}CD48^{-}CD41^{-}$ cells were shown to support LT multilineage reconstitution in the repopulation assay[26]. Utilizing Immunofluorescent staining with $Lin^{-}CD150^{+}CD48^{-}CD41^{-}$ markers, HSCs were confirmed to localize in the endosteal niche (~14-16%), but a large portion of these phenotypical HSCs (80-85%) were found within 5-cell distance from blood vessel, especially the sinusoid, thus the vascular

78 niche concept was formed[26,27]. Subsequently, numerous groups have contributed to
79 identification of various cell types that provide a niche function and these include
80 Cxcl12-Aboundandt Reticular (CAR) cells, Nonmyelin Schwann cells, Nestin$^+$, Prx1$^+$,
81 or Leptin receptor (LepR)$^+$ stromal cells, as well as megakaryocytes (Mks)[7,27-33]. Given
82 that the majority of stromal cells as described above are associated with vessels, and
83 the main components of which are the sinusoidal structure primarily found within the
84 CM covered by compact bone in the diaphysis region, the concept of the perivascular
85 niche predominantly confined within the CM has emerged[5]. Consistent with the
86 observation that 80-85% HSCs reside in the perivascular niche, deletion of *Cxcl12* or
87 *KitL* (or SCF) from vessel and vessel-associated stromal, such as LepR$^+$ or Prx1$^+$,
88 cells, led to a substantial (~85%) loss of HSCs[6,7,34]. However, the location and
89 characteristics of the remaining HSCs after the depletion of HSCs from the CM
90 remained largely unclear. The following observation seems to provide an answer:
91 myeloablation induced by the chemotherapy agent 5-fluorouracil (5-FU) resulted in a
92 significant loss of HSCs primarily residing in perivascular niches, whereas the
93 surviving, thus reserve, HSCs predominantly (~75%) found in the endosteal niche
94 within TBA[35].

95 Among the cell types reported with niche functions, accumulating evidence strongly
96 supports mesenchymal stem cells (MSCs) as pivotal in maintaining HSCs[28]. Several
97 MSC markers have been identified within BM, including Nestin, Prx1, and LepR [7,28,30].
98 While N-cad was the first identified niche marker in BM, the characteristic of N-cad$^+$
99 stromal cells was not fully understood until they were revealed to possess the potential
100 to differentiate into not only osteoblasts but also adipocytes and chondrocytes, thus
101 validating N-cad as an MSC marker[35]. All the aforementioned studies shed light on
102 niche markers and factors, providing valuable insights into understanding FL-HSCs
103 and their interactions with niches.

104 While the FL primarily acts as a temporary site for HSC further maturation and
105 expansion, numerous studies have focused on identifying the cellular and molecular

106 components involved in supporting FL-HSC expansion. Previous investigations,
107 primarily utilizing histological staining, *in vitro* culture, and single-cell RNA sequencing
108 (scRNA-seq), have revealed complex interactions between FL-HSCs and various FL
109 cell types, including ECs, hepatoblasts, hepatic stellate (stromal) cells, perivascular
110 cells, and macrophages, mediated by diverse cytokines and chemokines[36-42]. Despite
111 the undeniable roles of different FL structure cells and hematopoietic cells in
112 supporting FL-HSCs, it still requires a systematic and comprehensive understanding
113 of the niches responsible for FL-HSC maintenance and expansion.

114 Histological imaging, while capable of showing cell positions, often revealing only a
115 limited set of markers. Single cell (sc)RNA-seq can provide an in-depth profile of gene
116 expression but lacks the ability to preserve the spatial information of each cell within
117 its original tissue context, making it challenging to comprehensively profile the HSC-
118 niche interactions and signaling. In contrast, high-resolution spatial transcriptomics
119 represents a promising and cutting-edge technology that integrates spatial information
120 with transcriptomic data[43]. This approach enables the profiling of gene expression
121 within their native spatial context, providing a powerful way to visualize gene
122 expression patterns within a tissue or organ with unprecedented detail[43,44]. Hence, in
123 this study, we employed high-resolution spatial transcriptomics, specifically the Slide-
124 seq V2 method[45], to generate a spatial transcriptomic cell atlas of the mouse FL.
125 Additionally, we utilized genetic approaches to validate our observations derived from
126 spatial transcriptomics. Our primary objective was to investigate the niches
127 responsible for maintaining and expanding FL-HSCs.

128 **Results**

129 **Single-cell RNA-seq reveals the transcriptomics of mouse fetal liver HSCs and**
130 **potential niche cells.**

131 To establish a comprehensive cell atlas of HSCs and other cell types in FL, we
132 conducted scRNA-seq of the mouse FL at E16.5. Given the rarity in the FL, we first
133 isolated HSCs using fluorescence-activated cell sorting (FACS) and then combined

134 them with CD45$^-$ non-hematopoietic cells and CD45$^+$ hematopoietic cells from the
135 E16.5 FLs for scRNA-seq analysis, resulting in a total of 62,236 collected cells[46].
136 Subsequently, we employed the Uniform Manifold Approximation and Projection
137 (UMAP) analysis to identify and classify 8 clusters of FL parenchymal cells and 22
138 clusters of hematopoietic cells (Fig. 1a). Through a differential expressed gene (DEG)
139 analysis, we uncovered marker genes specific to HSCs as well as potential niche cells
140 (Fig. 1b). Notably, we observed high expression levels of *Ifitm1*, *Hoxa7*, *Hoxa9*, *Cd27*,
141 *Kit*, and *Ltb* in E16.5 FL-HSCs. Additionally, we found that well-known HSC surface
142 markers, such as *Procr* (Epcr), *Ly6a* (Sca1), and *Slamf1* (CD150), were also enriched
143 in E16.5 FL-HSCs (Fig. 1c). We examined gene expressions in various potential niche
144 cell types, including MSCs, ECs, hepatoblasts/hepatocytes, megakaryocytes, and
145 macrophages. FL-MSCs displayed enrichment of *Pdgfrα*, *Pdgfrβ*, *Acta2*, and *Fgfr1*.
146 We then compared several known MSC markers in adult BM. *Nes (Nestin*) and *Cspg4*
147 (encoding Ng2) were previously reported to be expressed in arterial pericytes that
148 located in proximity to FL-HSCs and exhibited the ability to drive HSC expansion *in*
149 *vitro*[38]. Our data showed that only a subset of FL-MSCs expressed with either *Nes*
150 (39.87%) or *Cspg4* (Ng2) (10.66%). In fact, *Nes* was predominantly expressed in
151 endothelial cells. Similarly*, Lepr* was predominantly enriched in endothelial cells[30] and
152 barely detected in MSCs (0.71%) (Fig. 1d). We discovered that *Cdh2* (N-cad) was
153 highly expressed in MSCs (59.77%), an intermediate level in hepatoblasts, and low
154 level in a subset of hepatocytes, thus displaying an expression pattern largely
155 overlapping with that of *Cxcl12* in MSCs (75.00%) and hepatoblasts, but apart from
156 hepatocytes (Fig. 1d,e). Additionally, other Niche factors, such as *Kitl* and *Igf2,* were
157 found in both MSCs and hepatoblasts; but *Ptn and Thpo* were respectively detected
158 in MSCs and hepatoblasts.
159 We also conducted immunofluorescence staining to gain further insights into the
160 cellular structure of the PV region of E14.5 FL. We identified four major cell types in
161 the peri-PV region: inner layer comprised of Endomucin$^+$/CD31$^+$ ECs; the outer layer
162 consisted of N-cad^{High}Pdgfrα$^+$ MSCs; and surrounded by N-cad^{Int} Albumin$^+$
163 hepatoblasts. Notably, the majority of MSCs were observed adjacent to PV ECs in the

164 peri-PV region (Fig. 1f, Extended Data Fig. 1a-d). For comparison, Nestin expression
165 was detected in Endomucin^{+} ECs and a subset of N-cad^{High} MSCs (Extended Data Fig.
166 1e, f). Previously, FL stellate cells or perivascular mesenchymal cells with expression
167 of Desmin and Acta2 were shown to play a role in supporting FL-HSCs[40]. In line with
168 this report, our scRNA-seq and IF staining results revealed that N-cad^{Hi}MSCs
169 exhibited an enrichment of Desmin (Extended Data Fig. 1g, h). As a comparison, in
170 the distal-to-PV (distal, hereafter) region, the hepatic sinusoidal was comprised of
171 endothelial cells, hepatocytes, N-cad^{Int} hepatoblasts, and sporadically distributed N-
172 cad^{Hi}MSCs. The latter are not displayed as the perivascular pattern as seen in the PV
173 region (Extended Data Fig. 1i).
174 In summary, we have effectively generated a fully annotated single-cell resolution atlas
175 of the mouse FL, together with IF staining, we provided comprehensive insights into
176 the cellular architecture of FL structure cells in the peri-PV region (Fig. 1g), and the
177 sinusoidal structure at the distal region. Notably, our study unveils that N-cad-
178 expressing cells constitute the primary source of niche factors in mouse FL.
179
180 **High-resolution spatial transcriptomics identifies HSCs and niche cells in**
181 **mouse FL.**
182
183 To gain a comprehensive understanding of the interactions between HSCs and niche
184 cells, we employed Slide-seq V2, a high-resolution (10μm) spatial transcriptomic
185 technology in our study[45]. We collected two sections of E14.5 mouse FL, focusing
186 specifically on a region enriched with portal vessels, as previous studies have
187 suggested proximity of FL-HSCs to the PV structure (Fig. 2a, b, Extended Data Fig.
188 2a). Since Slide-seq had not been previously applied to mouse FL investigations, we
189 conducted quality control analyses by assessing raw reads, high-quality reads, and
190 exotic reads, and compared them with a previous study conducted on the mouse
191 hippocampus[44] (Extended Data Fig. 2b-e). Our Slide-seq data exhibited a median of
192 approximately 320 unique molecular identifiers (UMI) per bead (d=10μm) and a
193 median of around 240 genes per bead, with minimal reads corresponding to ribosomal

194 genes (Extended Data Fig. 2i-l). Initially, using UMAP analysis, we identified only 10
195 distinct cell clusters due to the lower UMI and gene reads compared to scRNA-seq
196 (Extended Data Fig. 2 f-g). To construct a comprehensive high-resolution spatial
197 transcriptomic atlas of the E14.5 mouse FL, we applied the Robust Cell Type
198 Decomposition (RCTD) algorithm to assign cell types to the beads based on
199 expression profiles derived from E14.5 scRNA-seq[47]. This supervised approach
200 facilitated the categorization of 28 cell types, including 24 hematopoietic cell types and
201 4 parenchymal cell types (Extended Data Fig. 2 h).
202 We initially detected the presence of signature genes associated with erythrocytes and
203 erythroblasts across the entire "puck"(a rubber-coated glass coverslip containing a
204 monolayer of randomly deposited, DNA barcoded beads)[43] (Extended Data Fig. 3a).
205 As anticipated, the signature genes specific to the main structural and functional cells
206 in the FL, such as hepatoblasts and their progeny hepatocytes, were predominantly
207 detected within the tissue-covered regions (Extended Data Fig. 3b). To investigate the
208 spatial distribution of FL cells and the interaction between HSCs and niche cells, we
209 assigned the beads as credible representatives of a specific cell type when the
210 enriched signature genes exceeded a certain threshold. For potential niche cells, we
211 first annotated hepatoblasts and hepatocytes using a threshold of 25%, which best
212 represented the spatial localization of these cell types on the puck (Extended Data Fig.
213 3c, d). Utilizing this threshold, we identified five potential niche cell populations on the
214 pucks, each displaying its distinct spatial distribution pattern. Specifically, hepatoblasts
215 and hepatocytes were major parenchymal cells in the liver responsible for supporting
216 structural and metabolic functions (Fig. 2c). Furthermore, we observed an enrichment
217 of MSCs in the PV region, consistent with our prior IF staining findings (Fig. 2d). Most
218 megakaryocytes and macrophages were distributed within the liver lobes. ECs either
219 resided on the border of the PV as PV-ECs or were dispersed within the lobe as
220 sinusoid ECs, most of them are localized at the distal region (Fig. 2 e-g). A total of 7
221 HSCs were identified on puck #1, and 5 HSCs were identified on puck #2 using a
222 threshold of 35% (Fig. 2h, Extended Data Fig. 3e). Previous studies have estimated
223 that the total number of FL-HSCs is ~500 at E14 and ~1100 at E15, and FL-HSCs are

224 enriched surrounding portal vessel[13,38]. Based on the thickness of our section (10um)
225 and an average of 6 FL-HSCs identified per section, we estimated that the total
226 number of FL-HSCs per E14.5 liver in our experiment is less than 1200, which is close
227 to previous findings. It is noteworthy that the majority of HSCs were found in close
228 proximity to MSCs within the PV regions (Fig. 2i, Extended Data Fig. 3f). Out of the 12
229 HSCs from both pucks, 7 were adjacent to MSCs, 5 were near ECs, 4 were close to
230 hepatoblasts, 1 was in proximity to megakaryocytes, and none were near
231 macrophages. To assess the significant enrichment of HSCs to niche cells considering
232 the variable abundance of niche cell types in the FL, we performed a permutation test
233 (see method). The results showed a significant enrichment of FL-HSCs near MSCs
234 and ECs compared to other cell types (Fig. 2j, Extended Data Fig. 3g). Furthermore,
235 to comprehensively explore the niche cells surrounding each HSC, we applied a
236 decomposition method to identify the niche cell identities on each bead within a radius
237 of 50μm or 30μm from each HSC. Our analysis consistently revealed that 8 out of 12
238 HSCs were located within a compartment enriched with MSCs, while 4 out of 12 HSCs
239 resided in a compartment enriched with hepatoblasts and hepatocytes. In fact, 6 out
240 of 12 HSCs tended to be in direct contact with MSCs. (Fig. 2k, Extended Data Fig. 4a-
241 e). Immunofluorescence staining subsequently provided visual evidence of close
242 spatial proximity between a $Lin^{-}CD48^{-}CD150^{+}$ HSC and the $N\text{-}cad^{Hi}$ MSCs as the outer
243 layer of PV, as well as the $CD31^{+}$ EC as the inner layer of PV (Fig. 2l).
244 To compare with a previous study that utilized the 10x Visium spatial transcriptomics
245 solution for investigating FL-HSCs[41], we employed the same method to three
246 consecutive slices from an E14.5 mouse FL, following the standard protocol[41]. The
247 10x Visium method yielded an average of 5,139 median UMI per spot (d=55μm) and
248 1,756 median genes per spot, which were substantially lower than those obtained with
249 SLIDE-seq (5,139 vs 320, d=55μm vs d=10μm; 1,756 vs 240, d=55μm vs d=10μm).
250 Initially, the 10x Visium analysis identified nine cell clusters (Extended Data Fig. 5a, b).
251 Consistently, MSCs were enriched in the PV region, exhibiting a gene enrichment
252 score of approximately 80%, while megakaryocytes were predominantly located in the
253 liver lobe region, with a gene enrichment score of around 30% (Extended Data Fig. 5c,

254 d). However, the 10x Visium approach identified an average of two binding spots per
255 section containing HSCs, with a gene enrichment score below 25% (Extended Data
256 Fig. 5e). Similarly, to Slide-seq findings, the majority (4 out of 6) of HSC-containing
257 binding spots were found adjacent to or overlapping with MSC-containing binding
258 spots.
259 In summary, our high-resolution Slide-seq approach facilitated the generation of a
260 comprehensive spatial transcriptomic map of the mouse FL at E14.5. In addition, the
261 anatomical delineation of the PV structure through IF staining depicted MSCs and ECs
262 respectively forming the outer and inner layers of PV. Collectively, our analyses
263 unveiled a significant enrichment (>50%) of FL-HSCs within the PV region, positioned
264 directly adjacent to MSCs and indirectly influenced by signaling emanating from ECs.
265 While the enrichment of FL-HSCs to hepatoblasts didn't reach statistical significance,
266 the abundance of the latter suggests a potential interaction between them.
267
268 **Slide-seq decodes HSC-niche interactions.**
269
270 To investigate the dynamics of FL-HSCs and niche cells across various developmental
271 stages, we performed unsupervised scRNA-seq clustering using a dataset comprising
272 50,804 cells obtained from FACS-sorted $CD45^+$ and $CD45^-$ populations at E14.5,
273 E16.5, and E18.5 (Fig. 3a, Extended Data Fig. 6a). The differential expression of
274 genes (DEG) analysis was conducted to identify representative genes of HSCs at the
275 three embryonic time points. Notably, at E18.5, FL-HSCs exhibited a higher proportion
276 of cycling cells, indicated by increased expression of *Mki67*, and decreased
277 expression of *Cdkn1c (p57)*, *H19,* and *Mpl*. Previous studies have shown roles of
278 *Cdkn1c (p57)*, *H19,* and *Mpl* in the maintenance of quiescent HSCs in the adult BM[48-
279 50]. Additionally, we observed upregulation of FL-HSC signature genes such as *Procr*,
280 *Hoxa9*, *Kit*, and *Mecom* during late gestation. However, genes associated with
281 differentiation, including *Flt3*, and *Tgfβr1*, also showed increased expression levels.
282 Consistently, we found a notable increase in the frequency of Pre-B and B cells,
283 accompanied by a decrease in the frequency of HSCs and megakaryocytes from

284 E14.5 to E18.5, which are consistent with the gradual increase of *Flt3* but decrease of
285 *Mpl* and *Tek*[20,50,51] (Fig. 3 b, c).
286 To explore the potential ligand-receptor interactions between niche cells and HSCs in
287 an unbiased manner, we utilized CellPhone DataBase (CPDB) analysis[52]. Specifically,
288 we focused on characterizing interactions between HSCs and potential niche cells,
289 including MSCs, ECs, hepatoblasts, megakaryocytes, and macrophages. Through
290 comprehensive analysis, we identified MSCs as the primary providers of ligands
291 involved in niche-HSC interactions. These included well-established niche signals
292 known to support HSC in the adult BM, such as *Cxcl12-Cxcr4*, *Cxcl12-Dpp4*, *Igf1-Igf1r*,
293 *Igf2-Igf2r*, *Dlk1-Notch1/2*, *Tgfβs-Tgfβrs*, *Ptn-Ptprs*, *Kitl-kit*, and *Wnt* signaling pathways.
294 Hepatoblasts shared most of the identified interactions with MSCs, apart from their
295 unique enrichment in the *Thpo-Mpl* signaling module with HSCs, suggesting their role
296 in supporting megakaryocyte fate. ECs shared several ligands with MSCs, including
297 *Bmp4-Acvr2b*, *Kitl-Kit*, *Igf1-Igf2r*, *Igf2-Igf2r*, *Tgfβ2-Tgfβr2/3*, and *Ptn-Ptprs, but* lacked
298 *Cxcl12-Cxcr4*, *Cxcl12-Dpp4*, and *Dlk1-Notch1/2* signaling modules. In fact, only N-
299 cad-expressing cells, including MSCs and hepatoblasts, exhibited a *Cxcl12-Cxcr4*
300 interaction, suggesting their role as major chemokine-releasing cells involved in HSC
301 homing and localization. Macrophages and megakaryocytes displayed several distinct
302 interactions respectively, including *Ifng-Ifitm1* and *Pf4-Cxcr3 respectively*, suggesting
303 their unique contributions to support FL-HSCs (Fig. 3d).
304 While CPDB offers a scRNA-seq-based method for predicting ligand-receptor
305 interactions between cell clusters, it lacks the ability to provide a spatial representation
306 of genuine cell-cell interactions within an anatomically organized tissue. To verify the
307 cell-cell interactions identified by CPDB analysis, we first employed a "projection"
308 model to enhance genes detected on slide-seq (Extended Data Fig. 6b). Next, we
309 assessed the "observed" expression profile of *Alb*, which ranked as the 3rd most
310 enriched gene on the puck and compared it with the "projected" expression profile.
311 The projection model effectively enhanced the expression level of *Alb* (Albumin) with
312 high fidelity (Extended Data Fig. 6c-f). Similarly, the expression profile of *Cxcl12*,
313 previously known to be enriched in MSCs, was significantly enhanced using the

314 projection model (Extended Data Fig. 6 g, h). We then utilized Slide-seq to examine
315 the spatial expression patterns of the ligand-receptor pairs predicted by CPDB
316 analysis. Based on the number of HSCs involved in ligand-receptor interactions with
317 niche cells, we defined these interactions as strong (involving at least 3 out of 7 HSCs,
318 Extended Data Fig. 7a, b, f, j), weak (involving 1 or 2 out of 7 HSCs, Extended Data
319 Fig. 7c, d, h, i), or no interaction (Extended Data Fig. 7e, j). Overall, MSCs exhibited
320 several strong interactions with HSCs, including *Cxcl12-Cxcr4*, *Ptn-Ptprs*, *Kitl-Kit*,
321 *Tgfβ2-Tgfβr2*, and *Dlk1-Notch1/2*. Additionally, MSCs displayed weak interactions
322 such as *Cxcl12-Dpp4*, *Flt3l-Flt3*, *Igf1/2-Igfr1/2*, *Tgfβ1-Tgfβr1*, *Tgfβ3-Tgfβr3*, *Bmp4-*
323 *Acvr2b*, *Bmp5-Bmpr2*, *Angptl2-Tie2*, *Wnt2-Fzd6*, and *Wnt5a-Celsr1/Fzd6/Ryk* (Fig.
324 3e-i, Extended Data Fig. 7k). These findings indicate that MSCs are a major source of
325 niche factors that maintain FL-HSCs in proximity.
326
327 **The depletion of Cxcl12 from N-cad-expressing cells leads to increased**
328 **frequency of HSCs exhibiting lineage-biased differentiation.**
329
330 It has been established that Cxcl12 serves a crucial niche factor for maintaining HSCs
331 in the adult BM, demonstrated by studies showing that the loss of Cxcl12 from BM
332 vessel and vessel-associated stromal cells resulted a large reduction of HSC
333 frequency[7]. Given our observation that *Cxcl12-Cxcr4* interactions predominantly occur
334 between HSCs and N-cad-expressing cells, including MSCs and hepatoblasts, we
335 generated a conditional *Cxcl12* knockout mouse model using the *Cdh2*^{CreERT}*;Cxcl12*$^{f/f}$
336 strain to investigate the role of Cxcl12 in the maintenance of HSCs in the FL (Fig. 4a).
337 Subsequently, we performed fluorescence-activated cell sorting assays to assess the
338 impact of Cxcl12 loss on the frequency of HSCs, B cells, and CD41^{+} megakaryocytes
339 (Extended Data Fig. 8a). Unexpectedly, conditional knockout of Cxcl12 from N-cad-
340 expressing cells resulted in a significant (approximately 2-fold) increase in HSCs when
341 normalized to CD45^{+} cells (~1.5-fold increase normalized to total liver cells) (Fig. 4b).
342 FL B cells were completely depleted upon loss of Cxcl12 (Fig. 4c). Conversely, the
343 number of megakaryocytes increased significantly (~2-fold) when normalized to

344 CD45$^+$ cells (Fig. 4d).

345 Consistently, scRNA-seq analysis revealed that the loss of Cxcl12 had a significant
346 impact on HSC proliferation as evidenced by increased HSC number and skewed
347 lineage differentiation. Specifically, there was an increased myeloid cell such as
348 megakaryocytes and their progenitors, Inversely, there were loss of common lymphoid
349 progenitors (CLPs) and B lymphocytes upon conditional knockout of Cxcl12 from N-
350 cad-expressing cells (Fig. 4e, f). DEG analysis showed that Cathepsin G (*Ctsg)*, *Mpo*,
351 Selectin L (*Sell)*, and *Tetherin* were increased in HSCs after Cxcl12 loss, providing the
352 molecular basis for an increase in HSC proliferation, mobilization, as well as an
353 increase in differentiation towards myeloid cells [53-56] (Fig. 4g). Moreover, Gene
354 ontology (GO) analysis revealed an enrichment of pathways related to NADH
355 regeneration and glycolysis in HSCs upon Cxcl12 loss (Fig. 4h). N-cad-expressing
356 cells, particularly MSCs together with ECs, hepatoblasts in the PV niche, are
357 responsible for maintaining FL-HSCs with their full lineage potential. DEG analysis of
358 MSCs revealed that MSCs in wild-type (WT) mice are enriched in *Igf1* and *Cxcl12*,
359 indicative of their supportive role in HSC maintenance[57] (Extended Data Fig. 8b).
360 Subsequently GO analysis indicated that MSCs in WT mice are enriched in pathways
361 related to extracellular matrix organization and collagen fibril organization, suggesting
362 that extracellular remodeling by MSCs may create a favorable microenvironment with
363 appropriate geometric and mechanical properties to harbor HSCs[58] (Extended Data
364 Fig. 8c). In contrast, MSCs in conditional knockout (cKO) mice lost the enrichment of
365 extracellular matrix organization pathways, indicating an unfavorable extracellular
366 matrix microenvironment for HSCs harbor (Extended Data Fig. 8d).

367 Based on the CPDB analysis, the predicted significant ligand-receptor signaling from
368 MSCs to HSCs, including *Dlk1-Notch1/2*, *Ptn-Ptprs*, *Cxcl12-Cxcr4*, *Cxcl12-Dpp4*, and
369 *Igf1-Igf1r*, were reduced following the cKO of *Cxcl12*. Of particular note, the *Flt3l-Flt3*
370 signaling module between MSCs and HSCs was lost, most likely responsible for loss
371 of CLP and downstream B cells[59]. Several other ligand-receptor signaling interactions
372 between potential niche cells and HSCs were also found to be reduced, such as *Pf4-*
373 *Cxcr3* and *C5ar1-Rps19* between Megakaryocyte and HSCs, *Igf1-Igf1r* and *C5ar1-*

374 *Rps19* between Kupffer cells and HSCs, and *Cxcl12-Cxcr4* between hepatoblasts and
375 HSCs. Furthermore, *Tgfβ* signaling was predicted to be increased in hepatoblasts/
376 hepatocytes and Kupffer cells, while *Thpo-Mpl* signaling was increased in
377 hepatoblasts/hepatocytes, suggesting their involvement in skewed myeloid
378 differentiation[60,61]. Moreover, endothelial cells showed an increase in *Sirpa-Cd47*
379 signaling, implying the potential involvement of immune privilege pathways to
380 safeguard FL-HSCs against macrophage clearance and potentially contribute to HSC
381 expansion[62] (Extended Data Fig. 8e).
382 To further investigate the functional significance of Cxcl12 originating from N-cad-
383 expressing cells in HSC maintenance, we isolated FL-HSCs from both WT and *Cxcl12*-
384 cKO mice and transplanted them into WT adult recipient mice, which possess a normal
385 expression of Cxcl12 from N-cad-expressing cells. Following 16-week period, we
386 observed that the recipient mice exhibited balanced lineage reconstitution, indicating
387 that the observed lineage bias resulted from *Cdh2*^{CreER} induced *Cxcl12* depletion in
388 the FL was a niche-dependent phenotype (Fig. 4i).
389
390 **The absence of Cxcl12 from N-cad-expressing cells results in the altered**
391 **localization of HSCs to distinct niches.**
392
393 As Cxcl12-Cxcr4 is a recognized chemoattractant factor, we anticipated that the loss
394 of Cxcl12 from N-cad-expressing cells including mainly MSCs and hepatoblasts (Fig.
395 1d) would lead to an altered localization of of HSCs. To test this, we employed Slide-
396 seq using two FL sections from E16.5 WT and *Cxcl12*-cKO mice, respectively.
397 Compared to the HSC distribution pattern in E14.5 mouse FL, although distribution of
398 HSCs increased in the distal region, ~50% of HSCs are still in the PV region and
399 located close to MSCs in E16.5 FL (Fig. 5a). Intriguingly, depletion of Cxcl12 from N-
400 cad^{+} cells resulted in the relocation of HSCs initially located at the PV niche to the
401 distal region of fetal live (Fig. 5b). Specifically, in WT mice, 50% ± 23% of 36 HSCs
402 were found within 50μm of MSCs, whereas, in *Cxcl12*-cKO mice, only 13% ± 3% HSCs
403 were in proximity to MSCs. Similarly, in WT mice, 73% ± 9% of HSCs were close to

404 ECs, compared to 38% ± 9% HSCs in *Cxcl12*-cKO mice (Fig. 5c, d). To assess the
405 significance of HSC enrichment in proximity to various niche cells, we conducted a
406 permutation test. The data revealed that HSCs in WT mice were significantly enriched
407 in proximity to MSCs and ECs, whereas HSCs in *Cxcl12*-cKO mice did not show such
408 enrichment. Although the frequency of HSCs in proximity to ECs decreased after
409 Cxcl12 knockout, it did not change significantly between WT and cKO mice (Fig. 5e,
410 Extended Data Fig. 9a). These findings suggest that the relocation of HSCs away from
411 MSCs and remain interaction with ECs at the distal regions, where enriching sinusoids
412 (Fig. 1f). It is possible that hepatocytes remain relatively higher Cxcl12 level (Fig.1e)
413 in mutant FL when Cxcl12 was depleted from N-cad relatively higher expressed MSCs
414 and hepatoblasts (Fig.1d), which however requires a verification.
415 Since FL-HSCs predominantly undergo proliferation, we further subclustered the
416 E16.5 HSCs into cycling and non-cycling populations based on their gene expression
417 profiles from scRNA-seq (Extended Data Fig. 9b-d). The non-cycling HSCs exhibited
418 high levels of *Cdkn1c (p57)*, *Ctnnal1(α-catenin1)*, and *H19*, indicative of their
419 quiescent state. We then mapped the location of cycling and non-cycling HSCs in the
420 E16.5 FL (Extended Data Fig. 9e-h). The frequency of cycling HSCs was increased
421 upon Cxcl12 loss, which is consistent with the expansion of HSCs (Extended Data Fig.
422 10a).
423 Our findings indicate that the PV niche consisting of MSCs, ECs, and potentially
424 hepatoblasts in mouse FL plays a crucial role in maintaining relatively non-cycling
425 HSCs with full lineage potential. The loss of Cxcl12 from N-cad-expressing cells leads
426 to the altered location of FL-HSCs towards a distal sinusoidal niche, which comprises
427 ECs and potentially abundant hepatocytes but reraly MSCs (Extended Fig. 10d).
428 Occasionally, megakaryocytes and macrophages can also be part of sinusoidal niche.
429 The sinusoidal niche is pivotal in supporting proliferation of HSCs, albeit with a
430 myeloid-lineage bias.
431
432 **Dpp4^{+} but not Dpp4^{-} HSPCs predominantly homing to the trabecular bone area**
433 **in adults**.

434 We have focused on the analyses of the interaction between MSCs and FL-HSCs
435 through the Cxcl12-Cxcr4 axis, the CPDB analysis also revealed the interaction
436 between MSCs and HSCs involving Cxcl12 and Dpp4 (CD26) in mouse fetal liver (Fig.
437 3d). Dpp4 is a cell-surface protease known to cleave and deactivate various peptide
438 hormones and chemokines, including Cxcl12 as the top-ranked target, thereby
439 reducing its biological activity. This interaction can significantly influence the
440 chemotactic function of Cxcl12, impacting cell migration, mobilization, and homing of
441 stem cells[63,64]. However, it is difficult to study HSC-membrane associated Dpp4 as
442 there is neither known HSC-specific Cre mouse line nor robust HSC transplantation
443 assay system at the fetal stage.
444 To investigate Dpp4's role as a modulator in HSC migration and homing, we
445 transplanted $5x10^5$ total nucleated BM cells from Dpp4 WT ($Dpp4^{+/+}$-RFP) or Dpp4 KO
446 mT/mG mice ($Dpp4^{-/-}$-RFP) into WT recipients. Our findings indicated that Dpp4-WT
447 donor cells are notably enriched in the TBA region. Conversely, Dpp4-KO cells showed
448 a relatively lesser-extent and exhibit a more evenly distributed pattern (Extended Fig.
449 11a, b). Furthermore, Dpp4-WT cells localized closer to N-cadherin+ cells at the
450 endosteal niche compared to Dpp4-KO cells (Extended Fig. 11c).
451 Given Dpp4's inhibitory effect on the Cxcl12-Cxcr4 axis due to its enzymatic activity,
452 we hypothesized the presence of another factor in the endosteal niche modulating
453 Dpp4's activity. Previous studies have showed Glypican-3 (Gpc3) as an inhibitor of
454 Dpp4 function[65,66]. Indeed, we observed that enriched Gpc3 correlated with Cxlc12
455 protein level in the endosteal regions of TBA in mouse BM, presumably though
456 inhibiting Dpp4 and enhancing the Cxcl12-Cxcr4 signaling (Extended Fig. 11d). In
457 contrast, the central marrow has decreased level of Gpc3 but shows high levels of
458 Dpp4 expression primarily in $CD31^+$ endothelial cells (Extended Fig. 11e). The
459 combination of lower Gpc3, along with elevated Dpp4, in central marrow contributes
460 to the relatively lower gradient of Cxcl12 in CM compared to TBA, thus hindering HSC
461 homing.
462
463 **The absence of Cxcl12 from N-cad-expressing cells results in the altered**

464 **localization of BM HSPCs from the trabecular bone region to the central marrow**
465 **region.**
466 To further investigate how the Cxcl12-Cxcr4 axis influences HSC homing to the N-
467 cadherin+ niche, we conducted a bone marrow transplantation assay in adult mice.
468 This approach was chosen because transplantation into fetal mice presents significant
469 challenges. We transplanted $1x10^6$ total nucleated bone marrow cells isolated from
470 mT/mG mice into WT recipient (n=6), or the recipient with conditional knockout (cKO)
471 of Cxcl12 from N-cadherin-expressing cells (n=5). After 8 weeks, the femurs were
472 collected from both groups and those with intact BM on paraffin embedded sections
473 were used for IF staining of RFP to determine the distribution of transplanted donor
474 cells. The distribution of transplanted donor cells was significantly enriched in the
475 trabecular bone area (TBA, the knee joint side) in WT recipients, compared with the
476 central marrow (CM) area (TBA vs. CM, 52.98% ±8.26% vs. 13.62±4.10%). Upon
477 conditional knockout of Cxcl12 from N-cadherin-expressing cells, transplanted donor
478 cells increased homing to the CM from 13.62% (Wt) to 35.10% (mutant) (Fig. 5f, g).
479 FASC analysis of the bone marrow from both groups showed that the LSK cell number
480 was significantly increased in cKO mice compared to WT mice (9.49% vs 3.25%),
481 indicating that CM niche supports the proliferation of HSPCs (Fig. 5h). We further
482 conducted cell cycle analysis on the LSK cells in both groups. Data showed that in WT
483 mice, in which the majority of HSPCs reside in TBA area, 59.19% LSK cells are in G0
484 phase, 28.43% LSK cells are in G1 phase, and 7.74% LSK cells are in G2/S/M phase.
485 As a comparison, LSK cells in cKO mice exhibited a more proliferative profile, with
486 38.65% LSK cells are in G0 phase, 29.08% LSK cells are in G1 phase, and 25.42%
487 LSK cells are in G2/S/M phase (Fig. 5i).
488
489 **Discussion**
490 The journey of identifying and characterizing niches supporting HSCs has been
491 lengthy and intricate, marked by significant progress but often filled with conflicting
492 findings over the past decades. This complexity stems from both the complicated
493 nature of the BM system, and the influence of the single cell-based niche model,

494 resulting in a complex and controversial understanding of cell types crucial for HSC
495 maintenance and function[1-5].
496 The first niche discovered as supportive of HSCs in the adult mouse BM was the
497 endosteal niche, situated within the TBA[18,19]. This niche, composed of osteogenic
498 lineage or N-cad-expressing bone lining cells that now are recognized as MSCs[67], was
499 found to support LT quiescent HSCs[18,20,67]. Functional assays demonstrated the
500 crucial role of the endosteal niche in attracting homing of and supporting restoration
501 of HSCs in response to severe stress[35]. This aligns with the notion that the endosteal
502 niche predominantly supports a 'dormant' (deep quiescent) state of HSCs, functioning
503 as a reserve pool[18,22,68].
504 Subsequent studies uncovered additional HSC niches in the adult BM, including the
505 vascular niche, occupying 25% of the BM volume[69] and hosts 80-85% of HSCs[26,27].
506 Mature sinusoidal vessels, covered by compact bone in the diaphysis region,
507 associate various cell types in the perivascular region, contributing to niche
508 functions[7,20,27-31,67,70,71]. Deletion experiments targeting molecules like Cxcl12 or Kitl
509 from these vessels and vessel-associated MSCs, or myeloablation using 5-FU,
510 resulted in a significant (80-85%) reduction of HSCs, underscoring the importance of
511 these niches in supporting HSCs during homeostasis[6,7,34,35].
512 In contrast to the adult BM, FL-HSCs were thought to have unique proliferative
513 features, suggesting a distinct niche microenvironment[72]. Prior studies revealed
514 potential niche cell types in FL, including arteriolar ECs, PV-associated stroma cells,
515 and macrophages[38,41,42]. In this study, high-resolution spatial transcriptomics
516 uncovered existing two niches within different zones of FL: the PV niche, maintaining
517 quiescent HSCs with full lineage potential, and the sinusoidal niche, supporting
518 proliferative HSCs with a bias towards myeloid lineage. Loss of Cxcl12 from N-cad-
519 expressing niche cells altered HSC locations, leading to an "aging" phenotype with
520 increased proliferation but with myeloid bias.
521 These findings refine our understanding of FL-HSC niches and provide insights for
522 adult BM. Indeed, depletion of Cxcl12 from N-cad^{+} endosteal niche in adult BM altered
523 the location of HSPCs from initially being in the TBA to the CM, resulting in a reduction

524 in the G0 fraction of HSPCs. This is akin to the initial observation that Cxcr4$^{-/-}$ mice
525 exhibited a decreased G0 fraction of HSPCs, with HSPCs predominantly found in the
526 CM, leading to the previous conclusion that Cxcl12-Cxcr4 signaling induces
527 quiescence of HSPCs [27]. However, in this study, with Cxcl12 lost from N-cad-
528 expressing cells mainly in TBA, Cxcl12-Cxcr4 signaling between relocated HSPCs and
529 niche cells remained intact in CM, the increased HSPC proliferation is due to
530 microenvironmental differences between TBA and CM, rather than Cxcl12-Cxcr4
531 signaling *per se*. This revised interpretation offers a plausible explanation for why only
532 Prx1^{Cre} but not Lepr^{Cre} mediated Cxcl12 deletion resulted in substantial HSPC loss in
533 the BM and a significant increase in extramedullary hematopoiesis, despite
534 overlapping expression patterns of Prx1 and Lepr in the BM[6,7]. This discrepancy is
535 attributed to Prx1 initiating expression in the fetal stage, while Lepr is expressed only
536 in adult[73]. Thus, Prx1^{Cre} but not Lepr^{Cre} mediated Cxcl12 deletion altered the Cxcl12
537 gradient between the BM and extramedullary hematopoietic sites at the fetal-adult
538 transition stage, affecting neonatal homing of HSPCs to BM and subsequently
539 reducing adult BM HSPCs. Similarly, this also account for why Ng2^{Cre} mediated, but
540 not Ng2^{CreEr} induced, Cxcl12 deletion led to a decrease in the G0 fraction of HSPCs[74].
541 Our study, along with previous findings, has led us to propose a new model featuring
542 two distinct niches with multiple cellular components in different zones. The TBA
543 includes N-cad^{+} MSCs, osteogenic cells, various ECs, neural cells, supporting deep-
544 quiescent HSC[75,76]. The CM includes sinusoidal ECs, vessel-associated MSCs,
545 Schwann cells, and MKs, supporting heterogenous including relatively active
546 HSPCs[7,20,27-31,67,70,71]. TGFβ1 from MKs, activated by Schwann cells, maintains a
547 short-term quiescent state of HSCs during homeostasis but supports HSC restoration
548 post BM injury via FGF signaling [29,31,33,61]. Imaging of myelopoiesis defined the
549 anatomy of normal and stress hematopoiesis near megakaryocytes[77].
550 In summary, spatial transcriptomics has significantly advanced our understanding of
551 HSC niche interactions. The new discovery about the interplay between Dpp4 and
552 Gpc3, which plays a critical role in establishing the gradient of Cxcl12 across FL and
553 BM, enhances our understanding of how the broad expression of Cxcl12 leads to the

554 specific homing of HSPCs in both the FL and BM. This comprehensive analysis
555 combining spatial transcriptomics, immunofluorescent imaging, and genetic
556 approaches, results in a paradigm shift regarding the niche concept, moving from
557 single cell-based to multicellular components within distinct zones as proposed
558 previously[78]. This shift reflects the intricate regulation of HSPCs in association with
559 their cycling states and metabolic activities according to the hematopoietic stages and
560 in response to varies stresses, offering valuable insights for hematopoietic
561 homeostasis, aging process, and leukemogenesis.
562

563 **ACKNOWLEDGMENTS**

564 We thank K. Ferro, K. Bae, F. Liu, Z. Yu, E. Hamilton, M. Treese, I. Dunwiddie, J.
565 Morrison, and M. Peterson, M. Miller for technical support. We would like to
566 acknowledge the Board Institute and Dr. Fei Chen's group for providing the Slide-seq
567 V2 pucks. We would like to acknowledge the generated data on the Illumina NovaSeq
568 6000 System at University of Kansas Medical Center's Genomics Core, which was
569 supported by following grants: NIH U54 HD 090216, P30 GM122731-03, and NIH
570 S10OD021743. This work was supported by the Stowers Institute for Medical
571 Research (SIMR-1004) and NCI-designated Kansas University Comprehensive
572 Cancer Center (P30 CA168524).
573

574 **AUTHOR CONTRIBUTIONS**: R.D. conceived the project, designed, and performed
575 experiments, analyzed data, and wrote the manuscript. H.L and J.R. performed
576 bioinformatics analysis. R.D., C.W., W.L., S.M., K.P., K.H., A.S, M.M., S.H., and Z.Y.
577 performed scRNA-seq, Slide-seq, immunofluorescence staining, 10X Visium
578 experiments, and imaging processing and analysis. X.C.H. and M.H. provided the
579 training. W.L., X.M., Z.Y., and M.E. provided technological support. M.E. performed
580 proof-reading of the manuscript. S.S., S.M., Y.W., A.P., J.H., J.U., and B.S. provided
581 technical assistance. X.K., X.C.H. and L.L. supervised the study and revised the
582 manuscript.

583 **DECLARATION OF INTERESTS**

584 The authors declare no competing interests.

585

586 **Method (main text):**

587 **Mice**

588 The mice utilized in this study were all housed in the AAALAC-accredited animal facility
589 located at the Stowers Institute for Medical Research (SIMR), and were handled
590 according to both SIMR and National Institutes of Health guidelines. All procedures
591 involving experimental animals were approved and authorized by the Institutional
592 Animal Care and Use Committee (IACUC) of SIMR. N-cad-CreER^T mice were
593 generated by Applied StemCell, Inc. To induce N-cad-CreER^T; Cxcl12 f/f mouse,
594 Tamoxifen (Sigma) was injected intraperitoneally to the pregnant mothers at 2mg per
595 injection at E10.5, E12.5, and E14.5. C57BL/6, Ptprc, and Cxcl12 floxed mice were
596 acquired from the Jackson Laboratory.

597 **Tissue preparation and handling**

598 FL tissue was received freshly harvested in 1x PBS and were individually submerged
599 in OCT to remove excess PBS. Tissues were moved to a cryo-mold with fresh OCT
600 and orientated in “tulip” orientation for transverse tissue sectioning. Tissue blocks were
601 then flash frozen at -70°C before sectioning (HistoChill, Novec™ 7000). Region of
602 interest (multiple portal/central vein openings on same plain) were identified prior to
603 tissue capture.

604 **ScRNA-Seq**

605 Dissociated cells in PBS + 2.5% FBS were assessed for concentration and viability
606 via a Luna-FL cell counter (Logos Biosystems). Cells deemed to be 75-98% viable
607 were loaded on a Chromium Single Cell Controller (10x Genomics), based on live cell
608 concentration. Libraries were prepared using either the Chromium Single Cell 3'

609 Reagent Kits v3 or the Chromium Next GEM Single Cell 3' Reagent Kits v3.1 (10x
610 Genomics) according to manufacturer's directions. Libraries were sequenced to a
611 depth necessary to achieve at least 18,000 mean reads per cell on an Illumina
612 NovaSeq6000 or Illumina NextSeq500.
613
614 **Slide-seq V2**
615 The Slide-seq pucks used in this study were generated and sequenced at the Broad
616 Institute (Cambridge, MA) by Dr. Fei Chen's group according to the methods and
617 Extended Data information provided in the Nature Biotechnology publication "Highly
618 sensitive spatial transcriptomics at near-cellular resolution with Slide-seq V2" [44]. The
619 spatial barcode sequencing file of the pucks were generated via monobase ligation
620 chemistry and provided by Dr. Chen's group to be used for later analysis. The tissue
621 was sectioned to 10 µm thickness and mounted directly onto the pucks using a
622 cryostat (CryoStar NX70). Subsequent library preparation was performed according
623 to manufacturer's directions for the Nextera XT kit (Illumina, FC-131-1096)
624
625 **10x Visium**
626 Four 10um-thick tissue sections were adhered to the barcoded spots within the four
627 individual capture areas of a 10x Genomics Visium Spatial Gene Expression Slide.
628 The tissue was permeabilized for 18 minutes then processed to create cDNA and next
629 generation sequencing libraries according to manufacturer's instructions for the
630 Visium Spatial Gene Expression Reagent and Slide Kits (10x Genomics, PN-1000189
631 and PN-1000188). Libraries were pooled at equal molar concentrations and
632 sequenced to a depth necessary to achieve at least 50,000 read pairs per tissue
633 covered spot on the Illumina NextSeq 500 instrument using a High Output flow cell.
634
635 **Flow Cytometry**
636 Cells from mouse FLs or recipient BM freshly collected in 1xPBS with 2.5% PBS. Cells
637 were then stained with surface markers for 30 min at 4°C and washed with PBS (with
638 2.5% FBS) trice. Cells were then stained with 7-ADD/DAPI for 5 mins on ice and then

639 analyzed by ZE5 (Bio-Rad) or sorted by S6 cell sorter (BD Biosciences). FAC express
640 software 7.0 was used for data analysis.
641 For cell cycle analysis, BM cells were fixed in 4% PFA at room temperature for 30min,
642 followed by surface marker staining for 30 min at 4°C. Cells were then incubated with
643 anti-Ki67 in 1xPBS+0.1% tween-20 overnight at 4°C, followed by DAPI staining for 5
644 min on ice and then analyzed by ZE5 (Bio-Rad).
645 Fluorescence-activated cell sorting was performed on S6 cell sorter (BD Biosciences)
646 for the enrichment of HSC and niche cells for scRNA-seq. $Cd150^+$, $EPCR^+$, $N\text{-}cad^+$,
647 $CD31^+$ cells were collected and pooled with $CD45^+$ and $CD45^-$ cell for scRNA-seq.
648

649 **Bioinformatics and Statistical analysis**

650 To determine whether certain niche cell types are in the same niche micro-
651 environment and in proximity to HSCs, we applied a permutation test. First, a fixed
652 number equal of beads are randomly selected from all beads for a given puck and
653 annotated as “pseudo” HSCs. The number of the “pseudo” HSCs are equal to the
654 number of “real” HSCs identified on each puck. Second, beads and their annotated
655 cell types within a 50um radius centered to the “pseudo” HSCs are identified. Finally,
656 the number of niche cells are counted with each of these micro-environments (50um
657 circle). This process was repeated 100 times, and the proportion of the number of
658 nearby niche cells that are more extreme than our observed one is calculated. This
659 proportion is the p-value showing how often the HPSCs and niche cells are in
660 proximity.

661 See Extended Data method for the full bioinformatics analytical methods.
662
663
664
665
666

Figures

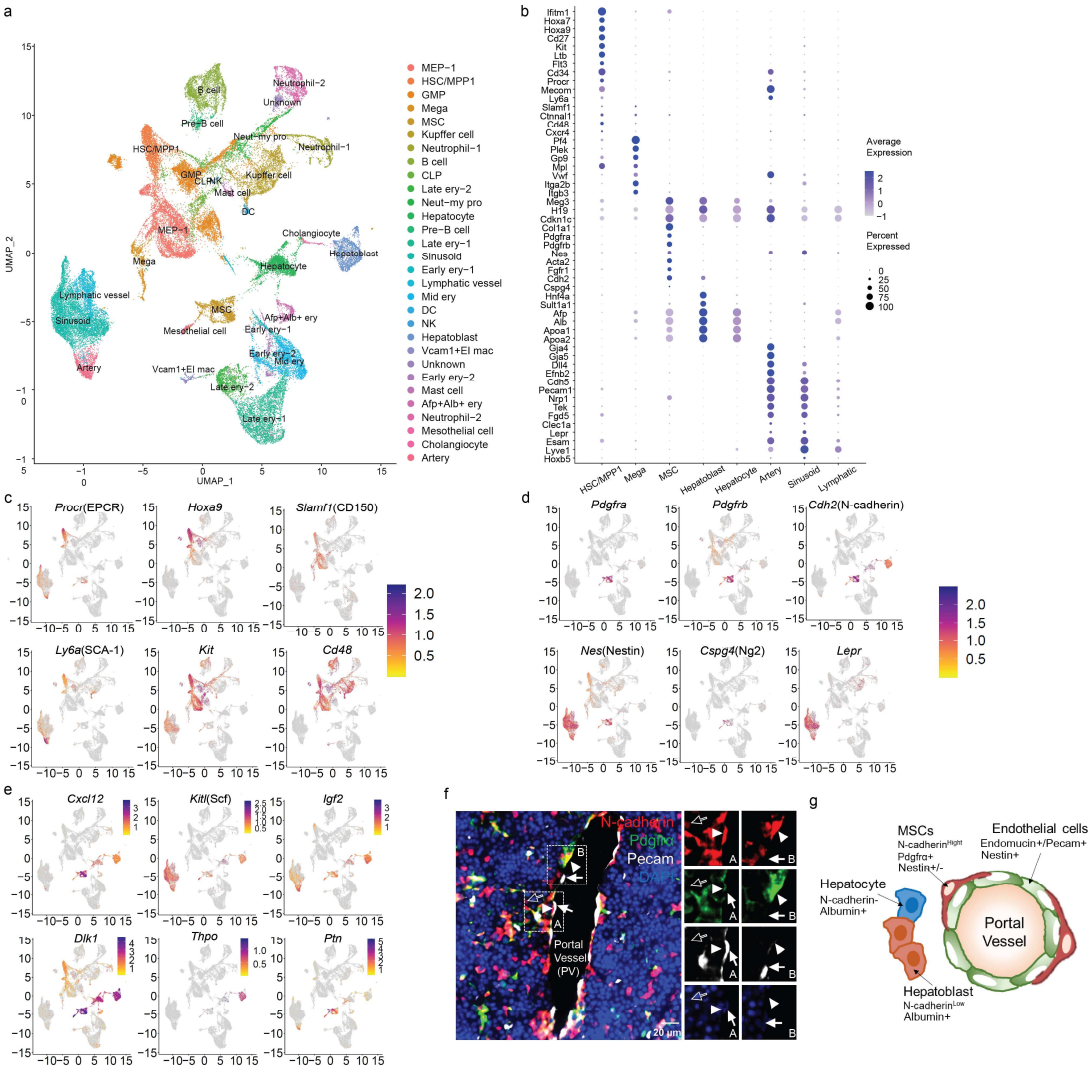

Fig. 1. scRNA-seq profiling of E16.5 mouse FL reveals markers for FL-HSCs and potential niche cells.

(a) UMAP visualization of E16.5 FL depicting distinct populations of HSCs and FL structure cells.

(b) Dot plot representation displaying marker genes for HSCs and potential niche cells.

(c) UMAP plot highlighting signature genes specific to HSCs.

(d) UMAP plot showcasing signature genes specific to FL structure cells.

(e) UMAP plot indicating the expression of niche factors in potential niche cells.

(f) Immunofluorescence staining demonstrating the cellular architecture surrounding a portal vessel. Solid arrow: Pecam1^{+} endothelial cells; Solid arrowhead: N-cad^{High}

679 Pdgfrα^{+} MSCs; Hollow arrow: N-cad^{Low} Hepatoblasts. Two peri-PV regions (A)(B) were
680 highlighted and zoomed on the right panels.
681 (g) Illustrations depicting the cellular architecture adjacent to a portal vessel.
682
683
684
685
686
687
688
689
690
691
692
693
694
695
696
697
698
699
700
701
702
703
704
705
706
707
708

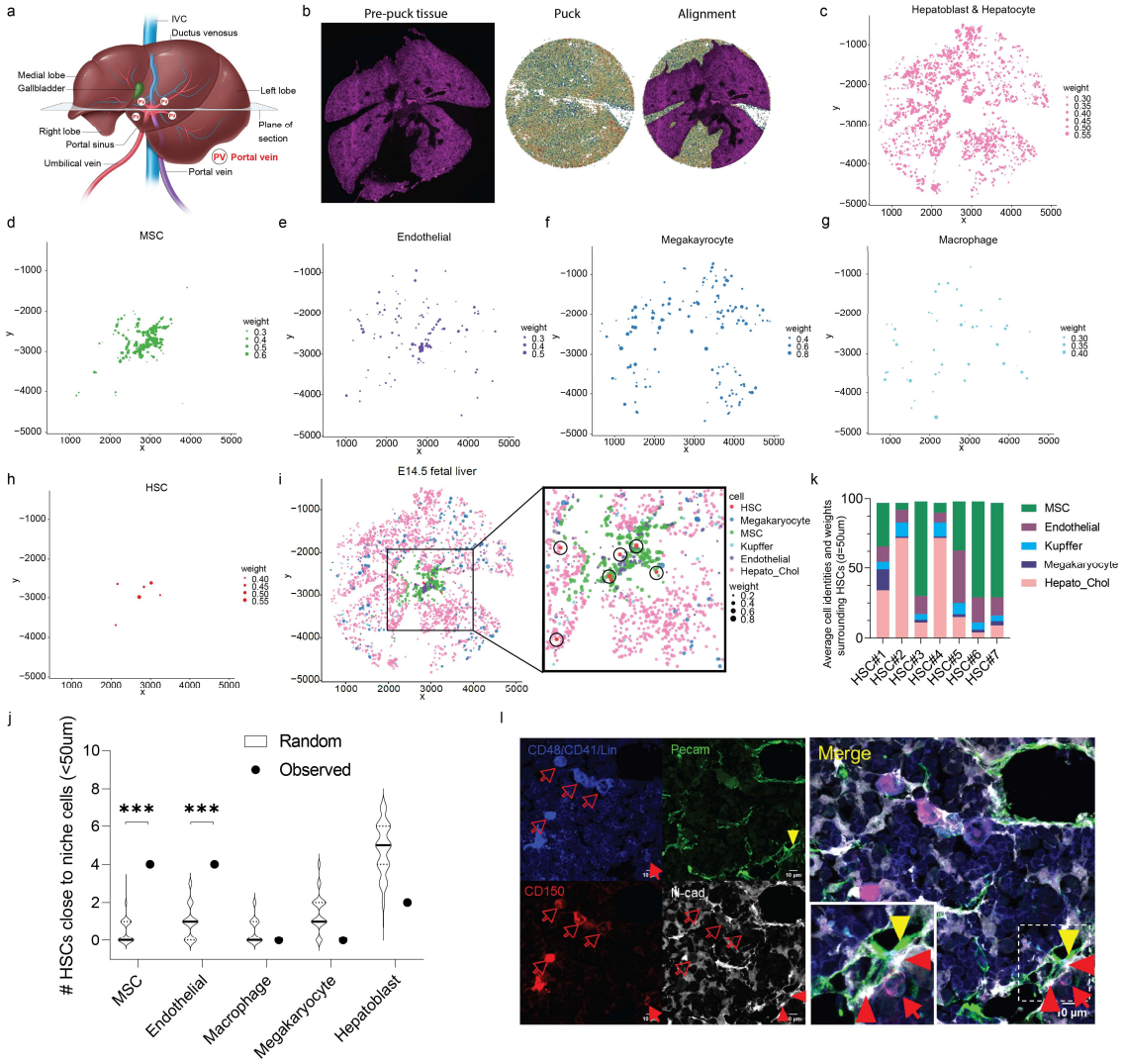

Fig. 2. Mapping cellular architecture and interactions in E14.5 mouse FL using Slide-seq.

(a) Illustrations depicting the mouse FL and plane of sections.

(b) DAPI staining on pre-puck section (left), the reconstructed SLIDE-seq puck post-sequencing (Middle), and the alignment of the tissue on the puck (Right).

(c)-(g) Identification of hepatoblasts & hepatocytes, MSCs, endothelial cells, megakaryocytes, and macrophages (Kupffer cells) using Slide-seq with a threshold of 25% (15% for endothelial cells).

(h) Identification of HSCs with a threshold of 35%.

(i) Cellular architecture of E14.5 mouse FL. Circles highlight the FL-HSCs.

(j) Permutation test demonstrating the enrichment of HSCs to potential niche cells.

721 The closest niche cell within 50μm to HSCs was considered as the niche cell to HSCs.
722 (k) Bar graph presenting the average cell identities surrounding each HSC from
723 puck#1 within 50μm. Decomposition was applied to all the beads surrounding each
724 HSC within 50μm. The weights of erythrocytes and erythroblasts were excluded on all
725 the beads.
726 (l) Immunofluorescence staining illustrating the HSCs-MSC interactions. Solid red
727 arrow: $CD150^{+}Lin^{-}CD48^{-}CD41^{-}$ HSC; hollow red arrow: $CD150^{+}LIN^{+}CD48^{+}CD41^{+}$
728 Hematopoietic progenitor and lineage cells; red arrowhead: N-cad^{High} MSCs; yellow
729 arrowhead: $Pecam1^{+}$ endothelial cells.
730 ***, $p<0.001$. showing combined p-value calculated using Fisher's combined
731 probability test
732
733
734
735
736
737
738
739
740
741
742
743
744
745
746
747
748
749
750

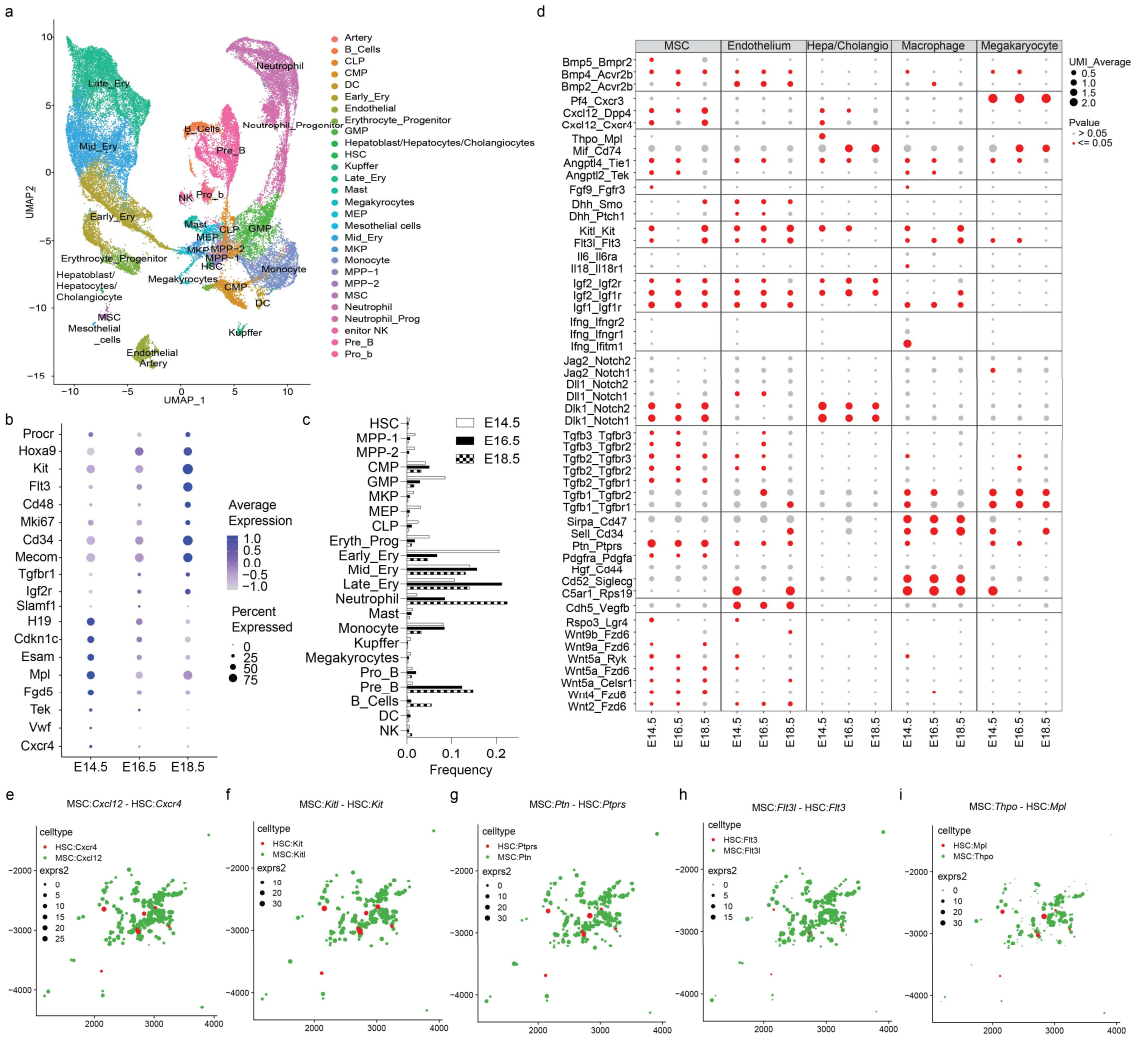

Fig. 3. Predicting ligand-receptor interactions between niche cells and HSCs using Cellphone DB and SLIDE-seq.

(a) Combined UMAP of mouse E14.5, E16.5, and E18.5 FL

(b) Dot plot illustrating the changes in HSC signature genes across mouse E14.5, E16.5, and E18.5 FL.

(c) Bar plot displaying the frequency of HSCs and lineage cells in mouse E14.5, E16.5, and E18.5 FL.

(d) Cellphone DB analysis predicting niche-HSC signaling in E14.5, E16.5, and E18.5 mouse FL.

(e) - (i) Slide-seq revealing the signaling interactions between MSCs and HSCs in E14.5 mouse FL.

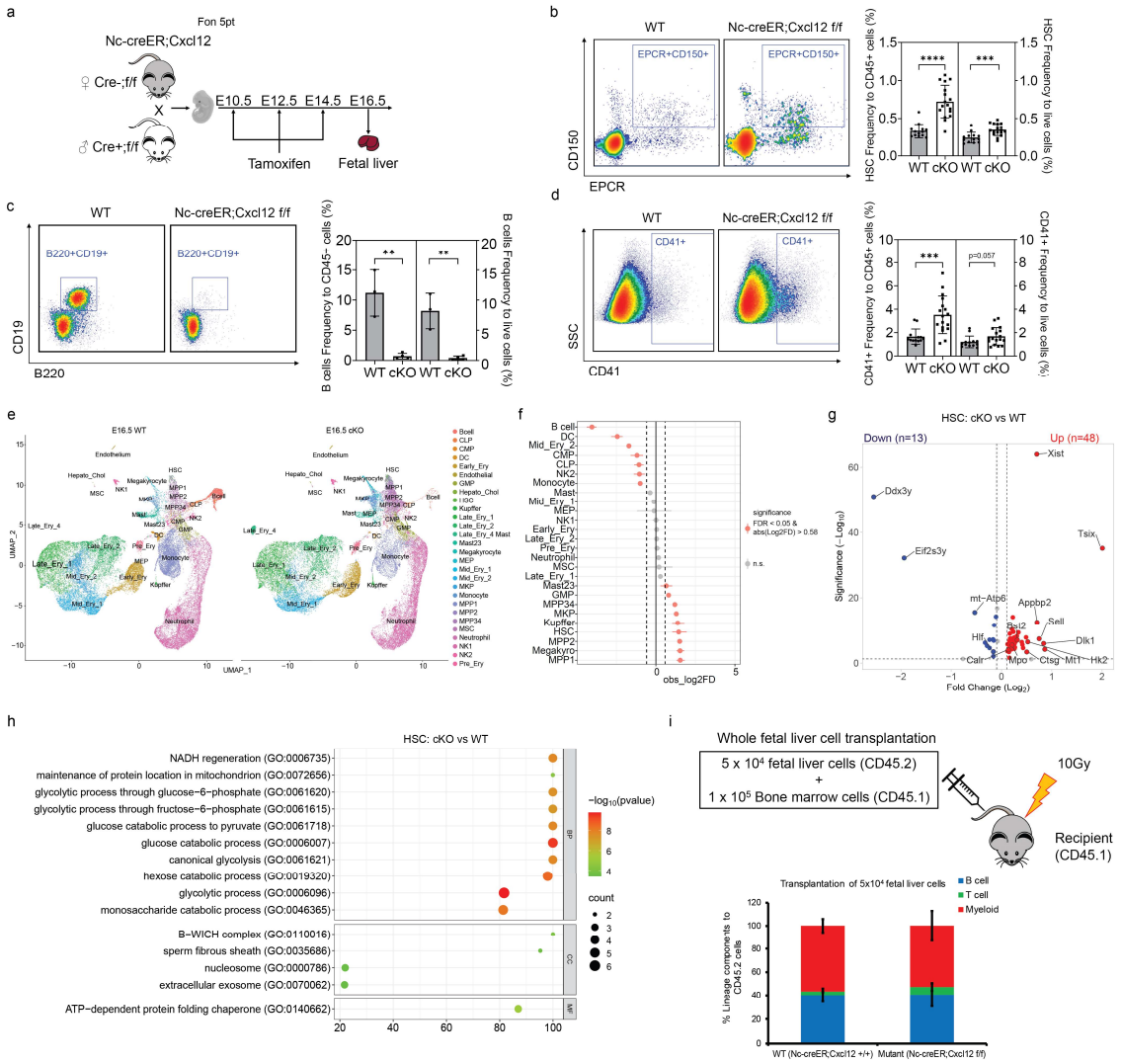

Fig. 4. Conditional knockout of Cxcl12 from N-cad expressing cells leads to HSC expansion with myeloid bias.

(a) Schematic overview of the experimental workflow.

(b) - (d) Representative FACS profiles and bar plots demonstrating the expansion of HSCs (b), depletion of B cells (c), and increased megakaryocytes (d) following the loss of Cxcl12 from N-cad-expressing cells.

(e) UMAP visualization of E16.5 mouse FL from wild-type (WT) and conditional knockout (cKO) mice.

(f) Bar plot indicating the skewed myeloid differentiation after the loss of Cxcl12 from N-cad expressing cells.

(g) Volcano plot displaying differentially expressed genes (DEGs) in HSCs mediated

775 by Cxcl12 cKO from N-cad-expressing cells.

776 (h) Bubble plot illustrating the top Gene Ontology (GO) terms in HSCs (BP: biological
777 process; CC: cellular components; MF: Molecular Functions) affected by Cxcl12 cKO
778 from N-cad-expressing cells.

779 (i) Bar plot showing the frequency of B cells, T cells, and myeloid cells in the recipient
780 BM 16 weeks post-transplantation.

781 *, $p<0.05$; **, $p<0.01$; ***, $p<0.001$. showing p-values calculated using student t's test.

782
783
784
785
786
787
788
789
790
791
792
793
794
795
796
797
798
799
800
801
802
803
804

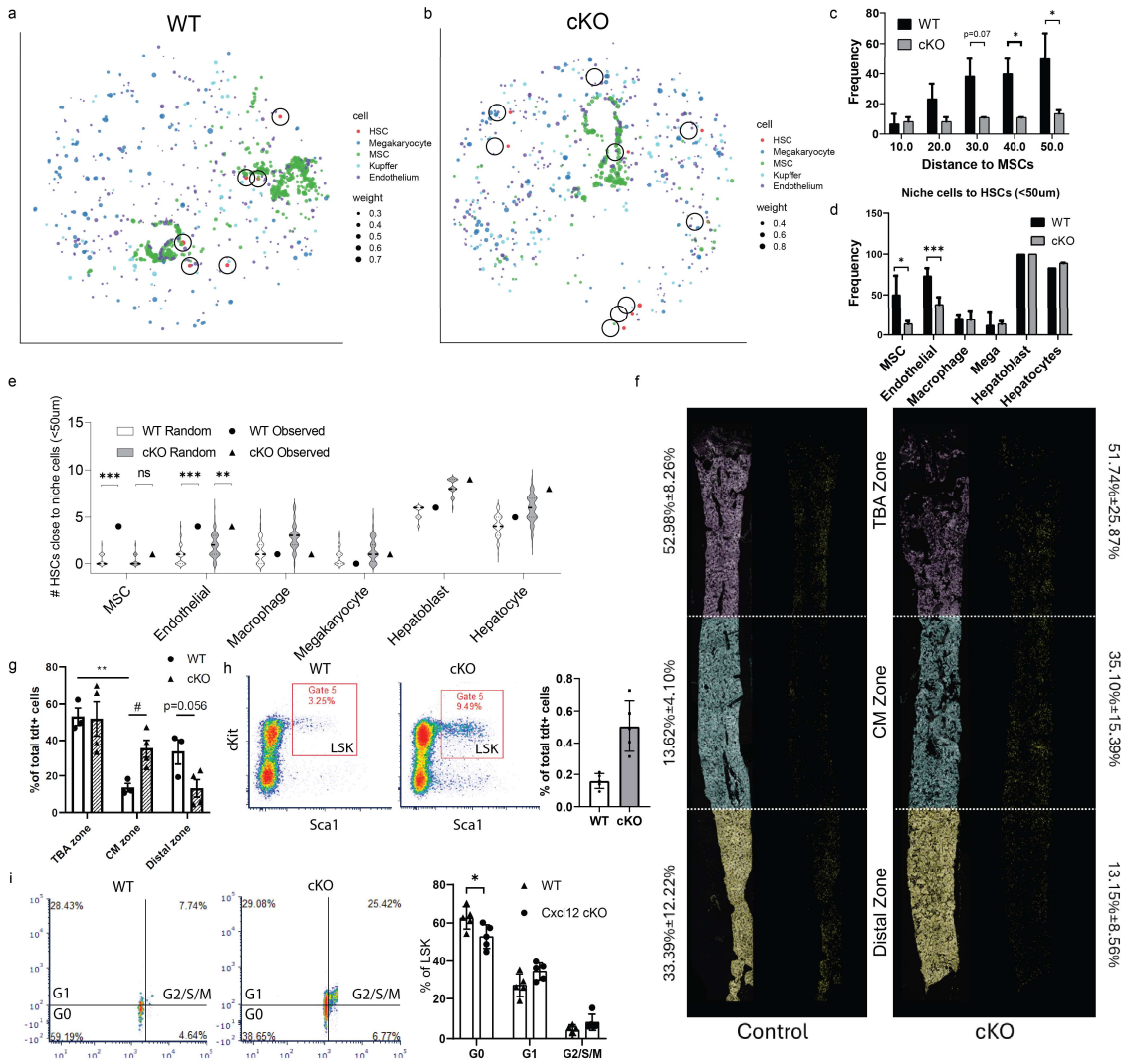

Fig. 5. Altered localization of HSCs in both FL and adult BM after conditional knockout of Cxcl12 from N-cad-expressing cells.

(a) (b) Slide-seq images displaying the cellular architecture in E16.5 mouse FL from wild-type (WT) (a) and conditional knockout (cKO) (b) mice (hepatoblasts and hepatocytes not shown).

(c) Bar plot illustrating the distances between HSCs and MSCs in WT and cKO mice.

(d) Bar plot indicating the significance of HSCs located within a distance of <50μm to niche cells in WT and cKO mice.

(e) Permutation test demonstrating the enrichment of total HSCs in proximity to potential niche cells in WT and cKO mice.

(f) Immunofluorescent staining of td-tomato showing the distribution of donor bone

817 marrow cells (from mT/mG mice) in the recipient bone marrow after 8 weeks. Left
818 images showing the segmentation of the bone (TBA zone vs. CM zone vs. Distal Zone).
819 Right images showing the td-tomato+ donor cells ausing anti-td-tomato IF staining.
820 (g) Bar plot indicating the distribution of td-tomato+ donor bone marrow cells in the
821 three different regions of recipient bone marrow.
822 (h) FASC analysis and bar plot showing the proportion of LSK cells in recipient bone
823 marrow in control vs cKO mice.
824 (i) FASC analysis and bar plot showing the cell cycle analysis of LSK cells in recipient
825 bone marrow in control vs cKO mice.
826
827 *, $p<0.05$; **, $p<0.01$; ***, $p<0.001$
828 (c)(d)(g)(h)(i) showing p-value calculated using student t's test.
829 (e) showing combined p-value calculated using Fisher's combined probability test
830 (g) showing p-value calculated using one-way ANOVA test.
831 #,$p<0.05$, (g) showing p-value calculated using student t's test.
832
833
834
835
836
837
838
839
840
841
842
843
844
845
846
847
848
849
850
851

852 **References**

853 1 Li, L. & Xie, T. STEM CELL NICHE: Structure and Function. *Annual review of cell and developmental*
854 *biology* **21**, 605-631 (2005).
855 2 Hoggatt, J., Kfoury, Y. & Scadden, D. T. Hematopoietic Stem Cell Niche in Health and Disease. *Annu Rev*
856 *Pathol* **11**, 555-581 (2016).
857 3 Torres, L. S. *et al.* Recent advances in "sickle and niche" research - Tribute to Dr. Paul S Frenette. *Stem*
858 *cell reports* **17**, 1509-1535 (2022).
859 4 Yang, Z., Dong, R., Mao, X., He, X. C. & Li, L. Stress-protecting harbors for hematopoietic stem cells.
860 *Current opinion in cell biology* **86**, 102284 (2024).
861 5 Morrison, S. J. & Scadden, D. T. The bone marrow niche for haematopoietic stem cells. *Nature* **505**, 327-
862 334 (2014).
863 6 Ding, L. & Morrison, S. J. Haematopoietic stem cells and early lymphoid progenitors occupy distinct
864 bone marrow niches. *Nature* **495**, 231-235 (2013).
865 7 Greenbaum, A. *et al.* CXCL12 in early mesenchymal progenitors is required for haematopoietic stem-
866 cell maintenance. *Nature* **495**, 227-230 (2013).
867 8 Weissman, I. L. & Shizuru, J. A. The origins of the identification and isolation of hematopoietic stem cells,
868 and their capability to induce donor-specific transplantation tolerance and treat autoimmune diseases.
869 *Blood* **112**, 3543-3553 (2008).
870 9 Müller, A. M., Medvinsky, A., Strouboulis, J., Grosveld, F. & Dzierzakt, E. Development of hematopoietic
871 stem cell activity in the mouse embryo. *Immunity* **1**, 291-301 (1994).
872 10 de Bruijn, M. F., Speck, N. A., Peeters, M. C. & Dzierzak, E. Definitive hematopoietic stem cells first
873 develop within the major arterial regions of the mouse embryo. *EMBO J* **19**, 2465-2474 (2000).
874 11 Kumaravelu, P. *et al.* Quantitative developmental anatomy of definitive haematopoietic stem cells/long-
875 term repopulating units (HSC/RUs): role of the aorta-gonad-mesonephros (AGM) region and the yolk
876 sac in colonisation of the mouse embryonic liver. *Development* **129**, 4891-4899 (2002).
877 12 Medvinsky, A. & Dzierzak, E. Definitive hematopoiesis is autonomously initiated by the AGM region. *Cell*
878 **86**, 897-906 (1996).
879 13 Ema, H. & Nakauchi, H. Expansion of hematopoietic stem cells in the developing liver of a mouse embryo.
880 *Blood* **95**, 2284-2288 (2000).
881 14 Christensen, J. L., Wright, D. E., Wagers, A. J. & Weissman, I. L. Circulation and chemotaxis of fetal
882 hematopoietic stem cells. *PLoS Biol* **2**, E75 (2004).
883 15 Gekas, C., Dieterlen-Lièvre, F., Orkin, S. H. & Mikkola, H. K. The placenta is a niche for hematopoietic
884 stem cells. *Dev Cell* **8**, 365-375 (2005).
885 16 Schofield, R. The relationship between the spleen colony-forming cell and the haemopoietic stem cell.
886 *Blood Cells* **4**, 7-25 (1978).
887 17 Crane, G. M., Jeffery, E. & Morrison, S. J. Adult haematopoietic stem cell niches. *Nat Rev Immunol* **17**,
888 573-590 (2017).
889 18 Zhang, J. *et al.* Identification of the haematopoietic stem cell niche and control of the niche size. *Nature*
890 **425**, 836-841 (2003).
891 19 Calvi, L. M. *et al.* Osteoblastic cells regulate the haematopoietic stem cell niche. *Nature* **425**, 841-846
892 (2003).
893 20 Arai, F. *et al.* Tie2/angiopoietin-1 signaling regulates hematopoietic stem cell quiescence in the bone
894 marrow niche. *Cell* **118**, 149-161 (2004).
895 21 Kokkaliaris, K. D. *et al.* Adult blood stem cell localization reflects the abundance of reported bone

896 marrow niche cell types and their combinations. *Blood* **136**, 2296-2307 (2020).
897 22 Wilson, A. *et al.* Hematopoietic Stem Cells Reversibly Switch from Dormancy to Self-Renewal during
898 Homeostasis and Repair. *Cell* **135**, 1118-1129 (2008).
899 23 Bernitz, J. M., Kim, H. S., MacArthur, B., Sieburg, H. & Moore, K. Hematopoietic Stem Cells Count and
900 Remember Self-Renewal Divisions. *Cell* **167**, 1296-1309 e1210 (2016).
901 24 Xie, Y. *et al.* Detection of functional haematopoietic stem cell niche using real-time imaging. *Nature* **457**,
902 97-101 (2009).
903 25 Lo Celso, C. *et al.* Live-animal tracking of individual haematopoietic stem/progenitor cells in their niche.
904 *Nature* **457**, 92-96 (2009).
905 26 Kiel, M. J., Yilmaz, O. H., Iwashita, T., Terhorst, C. & Morrison, S. J. SLAM family receptors distinguish
906 hematopoietic stem and progenitor cells and reveal endothelial niches for stem cells. *Cell* **121**, 1109-
907 1121 (2005).
908 27 Sugiyama, T., Kohara, H., Noda, M. & Nagasawa, T. Maintenance of the hematopoietic stem cell pool by
909 CXCL12-CXCR4 chemokine signaling in bone marrow stromal cell niches. *Immunity* **25**, 977-988 (2006).
910 28 Méndez-Ferrer, S. *et al.* Mesenchymal and haematopoietic stem cells form a unique bone marrow niche.
911 *Nature* **466**, 829-834 (2010).
912 29 Yamazaki, S. *et al.* Nonmyelinating Schwann cells maintain hematopoietic stem cell hibernation in the
913 bone marrow niche. *Cell* **147**, 1146-1158 (2011).
914 30 Zhou, B. O., Yue, R., Murphy, M. M., Peyer, J. G. & Morrison, S. J. Leptin-receptor-expressing
915 mesenchymal stromal cells represent the main source of bone formed by adult bone marrow. *Cell Stem*
916 *Cell* **15**, 154-168 (2014).
917 31 Zhao, M. *et al.* Megakaryocytes maintain homeostatic quiescence and promote post-injury regeneration
918 of hematopoietic stem cells. *Nat Med* **20**, 1321-1326 (2014).
919 32 Bruns, I. *et al.* Megakaryocytes regulate hematopoietic stem cell quiescence through CXCL4 secretion.
920 *Nat Med* **20**, 1315-1320 (2014).
921 33 Nakamura-Ishizu, A., Takubo, K., Fujioka, M. & Suda, T. Megakaryocytes are essential for HSC quiescence
922 through the production of thrombopoietin. *Biochem Biophys Res Commun* **454**, 353-357 (2014).
923 34 Ding, L., Saunders, T. L., Enikolopov, G. & Morrison, S. J. Endothelial and perivascular cells maintain
924 haematopoietic stem cells. *Nature* **481**, 457-462 (2012).
925 35 Zhao, M. *et al.* N-Cadherin-Expressing Bone and Marrow Stromal Progenitor Cells Maintain Reserve
926 Hematopoietic Stem Cells. *Cell Rep* **26**, 652-669.e656 (2019).
927 36 Chou, S. & Lodish, H. F. Fetal liver hepatic progenitors are supportive stromal cells for hematopoietic
928 stem cells. *Proc Natl Acad Sci U S A* **107**, 7799-7804 (2010).
929 37 Sugiyama, D., Kulkeaw, K., Mizuochi, C., Horio, Y. & Okayama, S. Hepatoblasts comprise a niche for fetal
930 liver erythropoiesis through cytokine production. *Biochem Biophys Res Commun* **410**, 301-306 (2011).
931 38 Khan, J. A. *et al.* Fetal liver hematopoietic stem cell niches associate with portal vessels. *Science* **351**,
932 176-180 (2016).
933 39 Tan, K. S., Kulkeaw, K., Nakanishi, Y. & Sugiyama, D. Expression of cytokine and extracellular matrix
934 mRNAs in fetal hepatic stellate cells. *Genes to Cells* **22**, 836-844 (2017).
935 40 Kordes, C., Sawitza, I., Götze, S. & Häussinger, D. Hepatic stellate cells support hematopoiesis and are
936 liver-resident mesenchymal stem cells. *Cell Physiol Biochem* **31**, 290-304 (2013).
937 41 Gao, S. *et al.* Identification of HSC/MPP expansion units in fetal liver by single-cell spatiotemporal
938 transcriptomics. *Cell Res* **32**, 38-53 (2022).
939 42 Lu, Y. *et al.* Spatial transcriptome profiling by MERFISH reveals fetal liver hematopoietic stem cell niche

940 architecture. *Cell Discovery* **7**, 47 (2021).
941 43 Rodriques, S. G. *et al.* Slide-seq: A scalable technology for measuring genome-wide expression at high
942 spatial resolution. *Science (New York, N.Y* **363**, 1463-1467 (2019).
943 44 Stickels, R. R. *et al.* Highly sensitive spatial transcriptomics at near-cellular resolution with Slide-seqV2.
944 *Nat Biotechnol* **39**, 313-319 (2021).
945 45 Marshall, J. L. *et al.* High-resolution Slide-seqV2 spatial transcriptomics enables discovery of disease-
946 specific cell neighborhoods and pathways. *iScience* **25**, 104097 (2022).
947 46 Weksberg, D. C., Chambers, S. M., Boles, N. C. & Goodell, M. A. CD150- side population cells represent
948 a functionally distinct population of long-term hematopoietic stem cells. *Blood* **111**, 2444-2451 (2008).
949 47 Cable, D. M. *et al.* Robust decomposition of cell type mixtures in spatial transcriptomics. *Nature*
950 *Biotechnology* **40**, 517-526 (2022).
951 48 Matsumoto, A. *et al.* p57 is required for quiescence and maintenance of adult hematopoietic stem cells.
952 *Cell Stem Cell* **9**, 262-271 (2011).
953 49 Venkatraman, A. *et al.* Maternal imprinting at the H19–Igf2 locus maintains adult haematopoietic stem
954 cell quiescence. *Nature* **500**, 345-349 (2013).
955 50 Yoshihara, H. *et al.* Thrombopoietin/MPL signaling regulates hematopoietic stem cell quiescence and
956 interaction with the osteoblastic niche. *Cell Stem Cell* **1**, 685-697 (2007).
957 51 Sitnicka, E. *et al.* Complementary signaling through flt3 and interleukin-7 receptor alpha is indispensable
958 for fetal and adult B cell genesis. *J Exp Med* **198**, 1495-1506 (2003).
959 52 Efremova, M., Vento-Tormo, M., Teichmann, S. A. & Vento-Tormo, R. CellPhoneDB: inferring cell–cell
960 communication from combined expression of multi-subunit ligand–receptor complexes. *Nature*
961 *Protocols* **15**, 1484-1506 (2020).
962 53 Florez, M. A. *et al.* Interferon Gamma Mediates Hematopoietic Stem Cell Activation and Niche
963 Relocalization through BST2. *Cell Rep* **33**, 108530 (2020).
964 54 Pellin, D. *et al.* A comprehensive single cell transcriptional landscape of human hematopoietic
965 progenitors. *Nature Communications* **10**, 2395 (2019).
966 55 Upadhaya, S. *et al.* Kinetics of adult hematopoietic stem cell differentiation in vivo. *J Exp Med* **215**, 2815-
967 2832 (2018).
968 56 Schroeder, T. & Just, U. Notch signalling via RBP-J promotes myeloid differentiation. *EMBO J* **19**, 2558-
969 2568 (2000).
970 57 Young, K. *et al.* Decline in IGF1 in the bone marrow microenvironment initiates hematopoietic stem cell
971 aging. *Cell Stem Cell* **28**, 1473-1482 e1477 (2021).
972 58 Oswald, J. *et al.* Gene-Expression Profiling of CD34+ Hematopoietic Cells Expanded in a Collagen I Matrix.
973 *Stem Cells* **24**, 494-500 (2006).
974 59 Sitnicka, E. *et al.* Key role of flt3 ligand in regulation of the common lymphoid progenitor but not in
975 maintenance of the hematopoietic stem cell pool. *Immunity* **17**, 463-472 (2002).
976 60 de Sauvage, F. J. *et al.* Stimulation of megakaryocytopoiesis and thrombopoiesis by the c-Mpl ligand.
977 *Nature* **369**, 533-538 (1994).
978 61 Challen, G. A., Boles, N. C., Chambers, S. M. & Goodell, M. A. Distinct hematopoietic stem cell subtypes
979 are differentially regulated by TGF-beta1. *Cell stem cell* **6**, 265-278 (2010).
980 62 Jaiswal, S. *et al.* CD47 is upregulated on circulating hematopoietic stem cells and leukemia cells to avoid
981 phagocytosis. *Cell* **138**, 271-285 (2009).
982 63 Christopherson, K. W., 2nd, Hangoc, G., Mantel, C. R. & Broxmeyer, H. E. Modulation of hematopoietic
983 stem cell homing and engraftment by CD26. *Science* **305**, 1000-1003 (2004).

984 64 Hoffmann, T., Faust, J., Neubert, K. & Ansorge, S. Dipeptidyl peptidase IV (CD 26) and aminopeptidase
985 N (CD 13) catalyzed hydrolysis of cytokines and peptides with N-terminal cytokine sequences. *FEBS Lett*
986 **336**, 61-64 (1993).
987 65 Davoodi, J., Kelly, J., Gendron, N. H. & MacKenzie, A. E. The Simpson-Golabi-Behmel syndrome causative
988 glypican-3, binds to and inhibits the dipeptidyl peptidase activity of CD26. *Proteomics* **7**, 2300-2310
989 (2007).
990 66 Khurana, S. *et al.* Glypican-3-mediated inhibition of CD26 by TFPI: a novel mechanism in hematopoietic
991 stem cell homing and maintenance. *Blood* **121**, 2587-2595 (2013).
992 67 Zhao, M. *et al.* N-Cadherin-Expressing Bone and Marrow Stromal Progenitor Cells Maintain Reserve
993 Hematopoietic Stem Cells. *Cell Rep* **26**, 652-669 e656 (2019).
994 68 Haug, J. S. *et al.* N-cadherin expression level distinguishes reserved versus primed states of
995 hematopoietic stem cells. *Cell stem cell* **2**, 367-379 (2008).
996 69 Nombela-Arrieta, C. & Manz, M. G. Quantification and three-dimensional microanatomical organization
997 of the bone marrow. *Blood Adv* **1**, 407-416 (2017).
998 70 Kunisaki, Y. *et al.* Arteriolar niches maintain haematopoietic stem cell quiescence. *Nature* **502**, 637-643
999 (2013).
1000 71 Kiel, M. J. *et al.* SLAM family receptors distinguish hematopoietic stem and progenitor cells and reveal
1001 endothelial niches for stem cells. *Cell* **121**, 1109-1121 (2005).
1002 72 Gao, S. & Liu, F. Fetal liver: an ideal niche for hematopoietic stem cell expansion. *Sci China Life Sci* **61**,
1003 885-892 (2018).
1004 73 Gao, L., Lee, H., Goodman, J. H. & Ding, L. Hematopoietic stem cell niche generation and maintenance
1005 are distinguishable by an epitranscriptomic program. *Cell* **187**, 2801-2816 e2817 (2024).
1006 74 Asada, N. *et al.* Differential cytokine contributions of perivascular haematopoietic stem cell niches.
1007 *Nature cell biology* **19**, 214-223 (2017).
1008 75 Shahrabi, S., Rezaeeyan, H., Ahmadzadeh, A., Shahjahani, M. & Saki, N. Bone Marrow Blood Vessels:
1009 Normal and Neoplastic Niche. *Oncol Rev* **10**, 306 (2016).
1010 76 Ho, Y. H. *et al.* Remodeling of Bone Marrow Hematopoietic Stem Cell Niches Promotes Myeloid Cell
1011 Expansion during Premature or Physiological Aging. *Cell stem cell* **25**, 407-418 e406 (2019).
1012 77 Wu, Q. *et al.* Resilient anatomy and local plasticity of naive and stress haematopoiesis. *Nature* **627**, 839-
1013 846 (2024).
1014 78 Weissman, I. L. Developmental switches in the immune system. *Cell* **76**, 207-218 (1994).
1015